Materials and Design 191 (2020) 108577

Contents lists available at ScienceDirect

Materials and Design

journal homepage: www.elsevier.com/locate/matdes

Development of carbon fiber acrylonitrile styrene acrylate composite for large format additive manufacturing

Daniel Moreno Sánchez [a,*], María de la Mata [a], Francisco Javier Delgado [a], Víctor Casal [b], Sergio Ignacio Molina [a]

[a] Departamento de Ciencia de los Materiales e Ingeniería Metalúrgica y Química Inorgánica, Facultad de Ciencias, IMEYMAT, Universidad de Cádiz, Campus Río San Pedro, 11510 Puerto Real, Cádiz, Spain
[b] Navantia S.A., S.M.E., Astillero Bahía de Cádiz, Polígono Astilleros s/n, 11519 Cádiz, Spain

HIGHLIGHTS

- Development and evaluation of CF / ASA composites. Rheological, thermal and mechanical characterizations.
- Large Format Additive Manufacturing (LFAM) 3D printing of ASA and ASA 20 wt.% CF.
- Influence of the printing direction (X and Z) on the mechanical properties.
- Fracture analyses addressed by means of optical and electron microscopies on neat ASA and ASA 20 wt.% CF printed pieces.

GRAPHICAL ABSTRACT

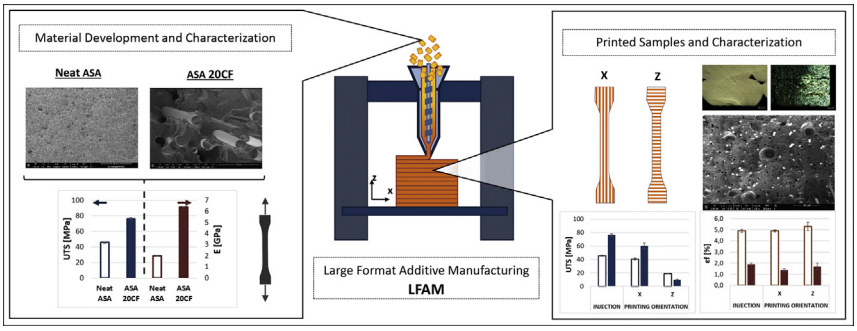

ARTICLE INFO

Article history:
Received 14 November 2019
Received in revised form 8 January 2020
Accepted 17 February 2020
Available online 21 February 2020

Keywords:
Acrylonitrile styrene acrylate (ASA)
Carbon fiber reinforced
Large format additive manufacturing (LFAM)
Big area additive manufacturing (BAAM)
3D printing
Fused filament fabrication (FFF)

ABSTRACT

The increasing interest of Large Format Additive Manufacturing (LFAM) technologies in various industrial sectors mainly lies on the attainable production of pieces reaching several cubic meters. These new technologies require the development of optimized materials with two-folded capabilities, able to satisfy functional in-service requirements but also showing a proper printability. Acrylonitrile Styrene Acrylate (ASA) is among the most interesting thermoplastic materials to be implemented in a LFAM device due to its excellent wettability and mechanical properties.

This research focuses on the development and characterization of ASA and carbon fiber (CF) ASA composites suitable for LFAM. The rheological, thermal and mechanical properties of neat ASA and ASA containing 20 wt% CF are addressed. The results evidence the higher performance of the CF loaded composite compared to the raw ASA polymer (i.e., the 20 wt% CF composite shows a 350% increase in flexural Young's Modulus and a 500% increment in thermal conductivity compared with neat ASA). Additionally, both materials were successfully printed along perpendicular directions (X and Z), showing the maximum tensile strain for the composite printed along the X orientation as was expected. The results of the flexural tests are comparable or slightly higher than those of injected parts. Finally, the fracture surface was analysed, identifying different types of porosity.

© 2020 The Authors. Published by Elsevier Ltd. This is an open access article under the CC BY-NC-ND license (http://creativecommons.org/licenses/by-nc-nd/4.0/).

* Corresponding author at: Departamento de Ciencia de los Materiales e Ingeniería metalúrgica y Química Inorgánica, Facultad de Ciencias, Universidad de Cádiz, Campus Río San Pedro Av., S/N, 11510 Puerto Real, Cádiz, Spain.
E-mail addresses: danielmoreno.sanchez@uca.es (D.M. Sánchez), maria.delamata@uca.es (M. de la Mata), fjavier.delgado@uca.es (F.J. Delgado), vcasal@navantia.es (V. Casal), sergio.molina@uca.es (S.I. Molina).

https://doi.org/10.1016/j.matdes.2020.108577
0264-1275/© 2020 The Authors. Published by Elsevier Ltd. This is an open access article under the CC BY-NC-ND license (http://creativecommons.org/licenses/by-nc-nd/4.0/).

1. Introduction

Additive manufacturing (AM) [1] has acquired an essential role in industry along the last decade, especially within Industry 4.0 [2,3]. Basically, the different technologies of additive manufacturing enable the creation of 3D pieces directly from digital models, by depositing the material layer-by-layer, for almost any shape (or even assembled), in different materials and in a batch as low as a unit [4–6].

Additive manufacturing, also known as 3D printing, includes a wide variety of technologies, classified into seven categories by the American Society for Testing and Materials (ASTM) attending to the material, physical state and the energy used during the printing process [7]. So far, the material extrusion related technologies are among the most studied as they offered a cost efficient and easily scalable alternative for a wide range of materials. By extrusion, the materials are deposited along lines following a toolpath, resulting in material layers which pile-up together to create the 3D pieces.

The pioneering work of Scott Crump, based on melting a feedstock filament deposited along a certain trajectory to create the 3D object, established the basis of thermoplastic material extrusion technology. He also founded the company Stratasys Ltd. and coined the term *Fused Deposition Modeling (FDM™)* to name this new technology [8], commonly named *Fused Filament Fabrication (FFF)* [9]. The typical printing built volume of these devices used to be about 0.5 m^3, imposing one of the main limitations for their employment in large format manufacturing. However, in recent years, new printing systems using thermoplastic polymer pellets as feedstock and a screw-extrusion system to melt and deposit the polymer, have significantly increased the printing volume (up to various cubic meters), while reducing the manufacturing time. Although due to the fast growth of the field there is not a standardized name for all those new technologies, they are usually referred as *Large Format Additive Manufacturing (LFAM)* [10–12]. Nonetheless, as it happened with FDM™, the commercial names are widely employed as, for instance, *Big Area Additive Manufacturing (BAAM)* and *Large Scale Additive Manufacturing (LSAM)*, developed by Cincinnati Incorporated and the Oak Ridge National Laboratory in 2014 [13] and Thermowood™ (both in USA), respectively.

The current state-of-art of the regarded technologies evidences their potential to be implemented in important industrial sectors, such as the automotive [14–16], the naval [12,17–19], construction [20–23] or energy [24–26], to produce faster prototypes, moulds, spare parts, or even final parts.

In spite of the above mentioned advantages, there are few limitations to be overcome. The laminar character of the FFF/LFAM processes, result in anisotropic properties of the obtained pieces in contrast to injected parts. In terms of the mechanical resistance, the printing direction is stronger (normally called as X-direction), while the weakest configuration is perpendicular (in-plane) to the deposition trajectory (known as Z-direction). This anisotropy might be tuned until some extend by increasing resistance along Z, for instance, by using a Z-tapping [27], Z-pinning [28,29] or preheating the surface with infrared lamps [30], plasma [31], laser [32] or microwaves [33].

Importantly, this technology requires from materials with a proper printability, while retaining their functionality, meaning low coefficient of thermal expansion (CTE), adequate melt flow index and high mechanical properties [12,34,35]. These requirements push the study and development of improved materials. One interesting strategy consists on combining different materials into a composite, to produce new or optimized materials with the sought properties. Different polymer composites are usually obtained by the addition of fibers (especially glass fibers, GF or carbon fibers, CF) playing a reinforcement role and reducing the CTE, which is fundamental to reduce warping or bending [36].

The most widely used thermoplastic in LFAM is *Acrylonitrile Butadiene Styrene (ABS)*, specially reinforced with 20% carbon fibers (CF) in weight (wt%), because of its high balanced properties of impact strength, stiffness, and processability [27,35,37]. Other technical materials such as, Polyphenylene Sulfide (PPS) [38], Polyphenylsulfone (PPSU) [10], Polyamide (PA) [15], Polyether Ether Ketone (PEEK) [39] or Polyethylene Terephthalate Glycol (PETG) [12] have been also tested in these technologies. However, their high cost and hard processability restrict their employment to few applications.

Acrylonitrile Styrene Acrylate (ASA) is an amorphous technical copolymer which has excellent UV properties, with good chemical resistant and high mechanical properties, widely used in automotive, gardening and other outdoor parts sectors with a feasible cost [40,41].

The chemical structure of ASA is schematically graphed in Fig. 1. It consists in rubber particles of alkyl acrylate (that works as impact modifier), compatibilized by a graft shell of poly (styrene-co-acrylonitrile) (PSAN), homogenously dispersed in a PSAN matrix [41].

Even though Jianbin Song et al. studied ASA CF [42] and the company Shanghai Construction Group has printed a 15.25 m long pedestrian bridge, using ASA reinforced with glass fiber [43], no research has been published using ASA as a base material for additive manufacturing.

In this research neat ASA and a developed ASA reinforced with carbon fiber were assessed and implemented in LFAM and study the influence in mechanical properties of printing orientation.

2. Materials and method

2.1. Materials

ASA Luran® S 777K from BASF (Germany) was used as thermoplastic base in this research. Not a commercial ASA CF is available, so as a reinforcing component, polyacrylonitrile (PAN)-precursor chopped carbon fibers Sigrafil® C30 from SGL Carbon (Germany) were used, with 3 mm length and 7 μm diameter. We have worked with two types of compositions, neat ASA and ASA-base composite with 20% of CF in weight (wt%). Hereinafter, we will refer to these materials as neat ASA and ASA 20CF, respectively.

With the intention to eliminate residual moisture that could interfere negatively during the manufacturing process, all the components and blends were dried in an oven for at least 4 h at 80 °C before any use.

In a first step, small amounts of ASA 20CF were blended in an internal mixer Rehoscam Scamex, (Fig. 2a), during 10 min, at 260 °C, at

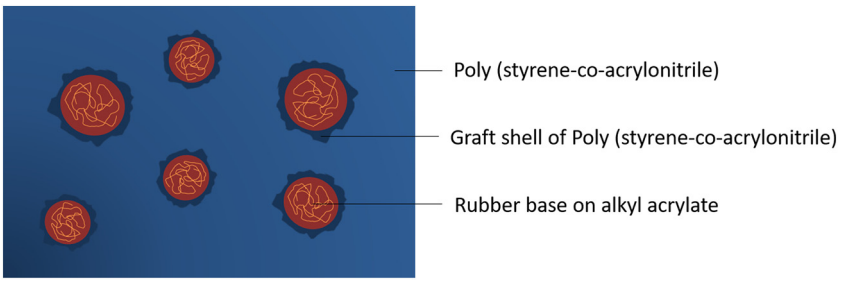

Fig. 1. Structure of ASA polymer.
Based on [41].

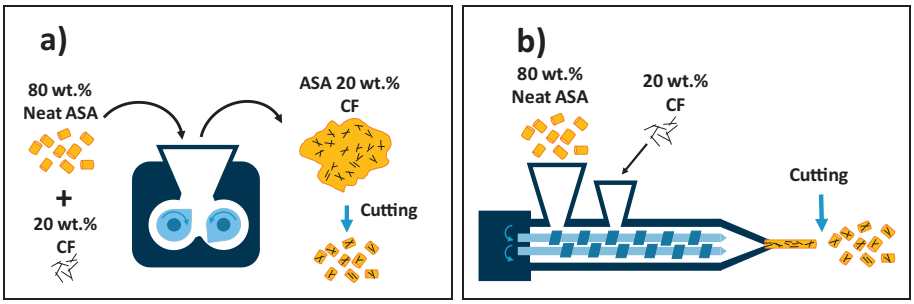

Fig. 2. Compound of ASA 20 CF a) small amount using an Internal Mixer; b) massive production using a Twin Screw.

50 rpm, intended for the creation of injected pieces for the composite characterization. At least 5 normalized tensile, 5 flexural test samples, 10 non-notched impact pieces and 2 thermal conductivity discs, of neat ASA and ASA 20CF were injected in a Babyplast 6/10 P and measured.

In a second step, after the evaluation and validation of the properties obtained, 30 kg of ASA 20CF were produced by a twin screw extruder SHJ (Fig. 2b), to be processed in the LFAM 3D printer. The twin screw was set at 300 rpm with the following temperature profile: 140-215-215-220-225-225-225 °C in the different zones of the barrel. The blended material was cut after extrusion in a blade mill WSGM–250, obtaining pellets of about 3–5 mm in length and 3 mm in diameter, following recommendations identified in bibliography for the extrusion process [44].

2.2. Printed samples

The studied samples were printed by using the Cartesian printer S-Discovery (Fig. 3) from CNC-Barcenas developed in a previous project [12] and located at Navantia Bay of Cadiz Shipyard. This large format 3D printer has a built volume of 3.5 m^3, with a vertical single-screw extrusion system attached to a gantry, which is directly fed with pellets delivered from a drier machine, and a heating bed. The extrusion system, with three heating zones, is able to reach up to 500 °C and the heating bed up to 120 °C.

In order to assess the degree of anisotropy of the printing process by determining the strongest and weakest mechanical resistance of the studied materials (neat ASA and ASA 20CF), flat samples of 420 × 300 × 5 mm^3 were printed along perpendicular directions (i.e., X and Z, shown in Fig. 4) using a 5 mm nozzle in diameter. The X-axis horizontal sheets have a height of 2 layers and do not have outer perimeter shell. The vertical sheets, called Z, contain one outer shell (perimeter) and consecutive sheets are joint together by an arc, creating a continuous toolpath to get vertical thin walls. A brim made of 5 beads at the first layer avoids the warping of vertical samples.

Fig. 3. S-Discovery LFAM device property of Navantia S.A., S.M.E. (placed at Bay of Cadiz Shipyard, Puerto Real, Cádiz, Spain).
Adapted from [12].

All the gcode files were generated using the slicer software Simplify 3D, widely used when working with FFF printers. The main parameters settled to fit the slicer to a single-screw extrusion system were a diameter nozzle and virtual filament diameter of 5 mm; a 2.5 mm layer height; a speed of 50 mm/s; heating bed at 110 °C; and 100% infill with 40% overlap. The temperature of the three zones of the barrel and the extrusion multipliers (EM) of each material, which allows managing the flow rate of different materials, are shown in Table 1. The values of these factors were determined using thermal and rheological characterization results of the materials and finely adjusted by the resulting dimensions and filling of printed blocks of 150 × 150 × 100 mm^3 for each material.

At least 5 tensile and flexural testing specimens were directly cut from the printed sheets, using a machining centre DMG Mori DMU 80 eVo. The cuts were aided with a tool developed and designed to avoid vibrations during the cutting process.

2.3. Characterization

In a first step, the neat ASA and ASA 20CF composite were characterized in terms of their mechanical, rheological and thermal properties. The mechanical properties were addressed by testing injected tensile, flexural and impact pieces. The melting flow rate (MFR) and the glass transition temperature (T_g), determined by differential scanning calorimetry (DSC), were measured for the two compositions. The thermal conductivity was measured using cylindrical injected discs.

In a second step, X and Z printed specimens were analysed by tensile and flexural tests, assessing the influence of the printing orientation in the mechanical properties of both, neat ASA and ASA 20CF.

Finally, the microstructure of the materials is analysed by means of optical and scanning electron microscopies. Specifically, tensile tested samples were study at the fractured surface of printed specimens aiming to discus and correlate microstructural features with differentiated mechanical performance of the two materials.

Rheological Characterization - The melting flow rate (MFR) of raw materials were measured in a plastometer Tinius Olsen MP600, following UNE–EN ISO 1133:2006 at 250 °C/10 kg.

Differential Scanning Calorimetry (DSC) - The glass transition temperature (T_g) of the materials was measured in a Metteler Toledo 1 Stare System.

Thermal Conductivity - The thermal conductivity was measured in a DTC-25. According to ASTM E1530, at least two injected discs of each material were measured.

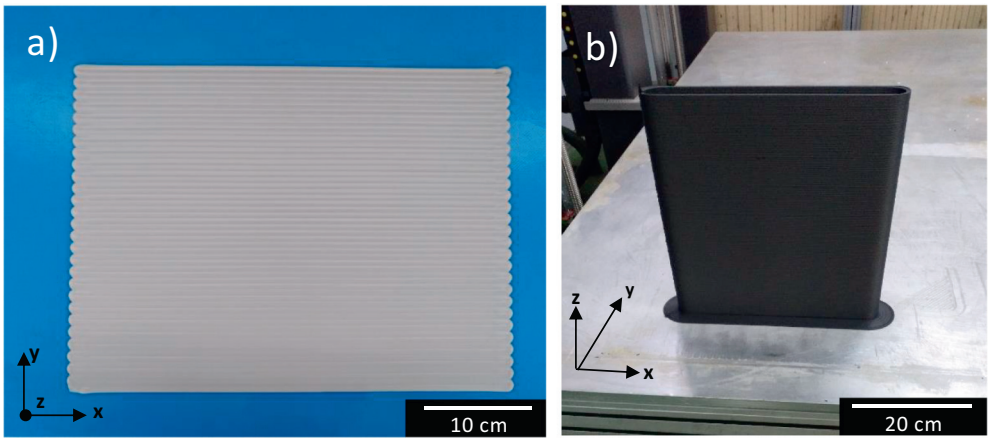

Fig. 4. Samples printed along the two different configurations studied: a) neat ASA sample printed along X direction outside the printer (XY plane displayed, being the Z-direction perpendicular to the image plane (outwards)); and b) ASA 20CF sample printed along Z direction inside the printer. X, Y and Z directions are indicated at the images.

Mechanical Characterization - Stress-strain curves were carried out at both, injected and printed parts at 2 mm/min in a Shimadzu AGS-X, in agreement with UNE–EN ISO 527 and UNE–116005:2012, respectively. UNE-116005:2012 considers the influence of orientation deposition. Charpy impact characterization of injected parts was performed using a Metrotest IMPats 2281, according to UNE–EN ISO 179 for non-notched specimens. Flexion characterization was carried out at 2 mm/min in a Tinius Olsen H10KS device following recommendations of UNE–EN ISO 178:2011.

Scanning Electron Microscopy (SEM) - A Nova NanoSEM 450 scanning electron microscope operated at 1.50 kV was used to characterize the fracture surfaces of the specimens. All printed parts were studied in X and Z orientations after tensile tests; On the other hand, two fractured samples of ASA 20CF were analysed (injected parts) in order to evaluate the interface between the fibers and the thermoplastic matrix (i.e., a cryogenic fragile fracture, induced at liquid nitrogen temperature and the standard fracture occurred in tensile test at room temperature).

Optical Microscopy - A Nikon SMZ-64 optical microscope was used in order to take fractographies of printed test tubes along X and Z orientations, for neat ASA and ASA 20CF.

3. Results and discussion

3.1. Materials characterization

Fig. 5 evidences the strong influence upon CF addition on the mechanical properties of the ASA, by comparing the strain-stress curves for both blends, neat ASA and ASA 20CF. The ultimate tensile strength (UTS) increases up to 67% and the Young's Modulus (E) reaches 223% while reducing the deformation or strain (ε) in a 95%, for the 20 wt% case, (Table 2). The SEM images included in Fig. 6 also indicate that the CF are well integrated within the polymer matrix, even after the tensile test, where the physical bonding remains incomplete pulled-out fibers. Jianbin Song et al. [42] explain this entanglement by the formation of chemical rings between the acrylonitrile and the surface of the CF precursor during blending, favoured after the surface oxidation of the CF precursor when undergoing the required temperatures for the process (200–300 °C [45,p.,39]).

Table 1
Printing parameters of samples created by LFAM.

	Extrusion temperature [°C]	Extrusion multiplier [%]
Neat ASA	250/255/255	0.54
ASA 20CF	240/260/260	0.86

These results are in good agreement with previous researches in which the addition of carbon fibers modifies the behaviour of the polymers into a brittle-like performance. During fracture, the propagation of the crazes is affected by the fibers pull-out; resulting in an increase of the ultimate tensile strength and Young's Modulus, while the strain is dramatically reduced [37,46,47]. Even assuming a perfect adhesion between the constituent phases, the smaller effective area of the polymer within the composite may explain the lower strain, as the plastic deformation of the CFs during the stress application must be also accounted.

It is worth to note that other blends with higher CFs loads tested (i.e., 30% wt. CF) have shown poorer mechanical improvements than that observed for ASA 20CF. The measured tensile behaviour and the T_g variation of ASA 30CF [48] show a slight increment of 5.5% (UTS) and 1 °C (T_g) compared with ASA 20CF, meaning 80.5 MPa and 112 °C, in UTS and T_g respectively. This poor increase on the mechanical properties using the same materials and procedure, might be attributed to the reinforcement saturation effect of the fibers. Thus, the mechanical improvement provided by the addition of higher CF amounts do not compensate the associated economic costs with commercial purposes. Moreover, the probability of the nozzle clogging is higher as the CF/polymer ratio is increased, involving a deeper optimization of the morphology of the fibers (i.e., optimized length), turning into a specific research work itself. Therefore, and in agreement with most reported works on LFAM of CF/polymer blends [27,35,37], in the following we have focused on neat ASA and ASA 20CF.

The impact test results in a great reduction of the absorbed energy (87%) by the 20 wt% CF composite as compared with the bare polymer (neat ASA). Therefore, it can be concluded that the new bonding between fibers and polymers does not compensate the reduction in effective area of the polymer.

The flexural properties are in agreement with the rest of the tests performed, evidencing the larger brittleness of the CF/ASA composite. The addition of 20 wt% CF results in a sharp increase in the ultimate flexural strength, UTSf (75%) and an increment of 350% in flexural Young's Modulus (Ef) is observed, while flexural strain (εf) decreases a 61%.

The measured MFR shows a flow reduction upon CF addition, as expected. During the MFR test, the amount of melt polymer decreases (44.7%) when increasing the CF percentage from 0 to 20%, due to the larger contact area between the fibers and the polymer, hindering the polymeric chains movement.

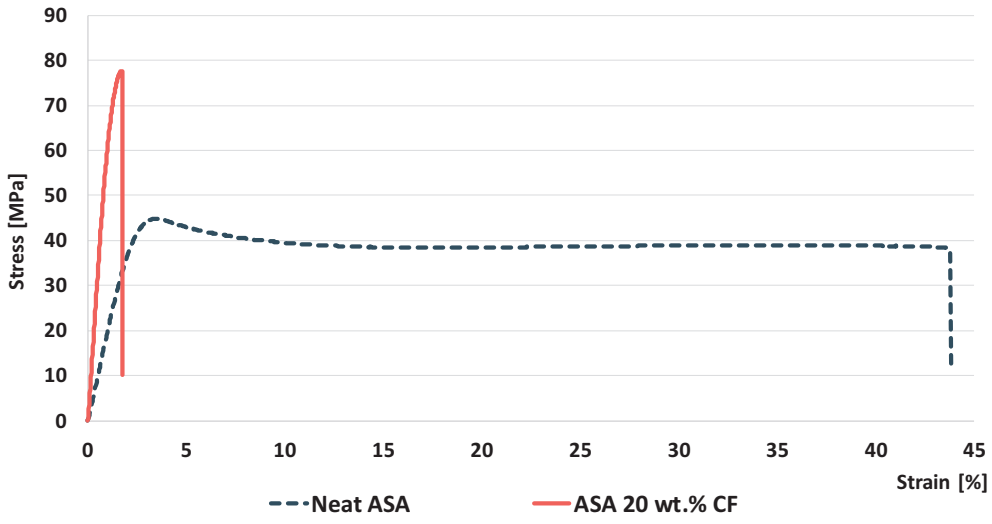

Fig. 5. Stress-strain curves of ASA blends.

Similarly, the observed increment of T_g between the unfilled and the filled polymer may be related to the polymer chain mobility (needing more energy those composites with higher loads to produce the thermal transition of the blend [42]). In addition, there is a significant increment of up to 500% in the thermal conductivity of the composite induced by the high thermal conductivity of the CFs, turning these polymers into highly attractive materials for applications such as moulding, while requiring an extra control of the cooling rate during the printing procedure.

Duty et al. reported that rheological and thermo-physical properties are the most important parameters to reach a proper polymer printability in LFAM [34]. From the rheological characterization it is possible to establish the optimum value of the extrusion multiplier during printing, usually used to compensate small variations between the filament diameter or the printers configuration, in our system EM allows to control the flow rate of the extruded material with different viscosity, preventing lack-or-excess material defects. On the other hand, the thermal characterization is crucial to set the printing temperature and the feed rate, that is, the maximum and minimum layer time available ensuring the bonding between successive beads, to prevent defects such as delamination, warping or drooping [49–52]. A printing temperature at least 120 °C over T_g is recommended [10].

3.2. Printed parts characterization

As it can be observed in Fig. 5, both, neat ASA and ASA 20CF, were successfully printed in our LFAM printer with no major issues. The discrepancies between the two EMs required for printing both materials studied (60% higher for ASA 20CF (Table 1)) denote the tight relationship of the EM parameter with the materials rheological properties. In our case, the EM value controls the material flow rate, connecting a variety of parameters involving the software managing procedure (i.e. virtual filament diameter or path overlap) and the printer device itself (i.e. spin-speed of the screw or temperatures of the barrel). The higher EM required for printing more viscous materials might be related to the higher spin-speed of the screw to move the fused material, in concordance with the above observed reduction of MFR by CF inclusion. Note that EM = 1 means that the flow rate and settings parameters are well balanced, while EM = 0.5 means that only 50% of the flow rate would be 'stablished' in the slicer. In our case, the lower values in both cases might lead to the underestimation of the deposited amount of material (the amount of extruded material by the printer might be more than the virtual filament of 5 mm in diameter).

Table 2
Mechanical, rheological and thermal properties of the studied neat ASA and ASA composite.

Properties	Units	Neat ASA	ASA 20CF
Tensile properties	UTS [MPa]	45.7 ± 0.9	76.3 ± 1.9
	ε [%]	41 ± 8	1.72 ± 0.13
	E [GPa]	1.98 ± 0.02	6.4 ± 0.1
Flexural properties	UTS_f [MPa]	52.6 ± 1.9	92 ± 2
	ε_f [%]	4.9 ± 0.1	1.9 ± 0.1
	E_f [GPa]	1.48 ± 0.05	6.7 ± 0.1
Impact	[kJ/m^2]	140 ± 30	18 ± 1
MFR	[g/10 min]	47	26
Tg	[°C]	103	111
Thermal conductivity	[W/mK]	0.17	0.90

UTS: Ultimate Tensile Strength; ε: Strain; E: Young's Modulus; UTS_f: Ultimate Flexural Strength; ε_f: Flexural Strain; E_f: Flexural Young's Modulus.

Table 3 shows the results obtained during the mechanical testing (tensile and flexural) of neat ASA and ASA 20CF for printed pieces along X and Z orientations. The error bars display the standard deviation of the measurements. Fig. 7 (tensile test) and Fig. 8 (flexural test) gather the mechanical results got on injected pieces, while SEM and optical images for both studied orientations are shown in Fig. 9 (neat ASA) and Fig. 10 (ASA 20CF).

As it is expected, all the printed pieces (neat ASA and ASA 20CF) present poorer mechanical performance than injected ones as a common trend, especially along Z orientation. For example, neat ASA shows a reduction of 11% and 58% in UTS for X and Z orientations respectively, as compared to injected pieces. The addition of CF leads to variations in UTS of 21% and 87% for X and Z, respectively, in the case of ASA 20CF. However, an increase of 12% in strain is noted when comparing injected and X orientated printed pieces made of ASA 20CF. Such increment would be explained by the preferential orientation of CF experimented during printing, which would need an extra displacement in order to pull out fibers from polymeric matrix during breakage [51].

In flexural test, however, the measured properties for printed samples are similar, even slightly superior, than for injected ones, mainly those printed along X orientation for neat ASA. Probably, the laminar character, compressive residual stress and preferential alignment of the polymer chains for those parts might improve the mechanical properties against flexural load application.

The reinforcement behaviour of the CF in injected pieces compared with printed neat ASA (in X orientation) is clear in both, tensile and flexural tests. An improvement of 220% and 157% is observed in Young's

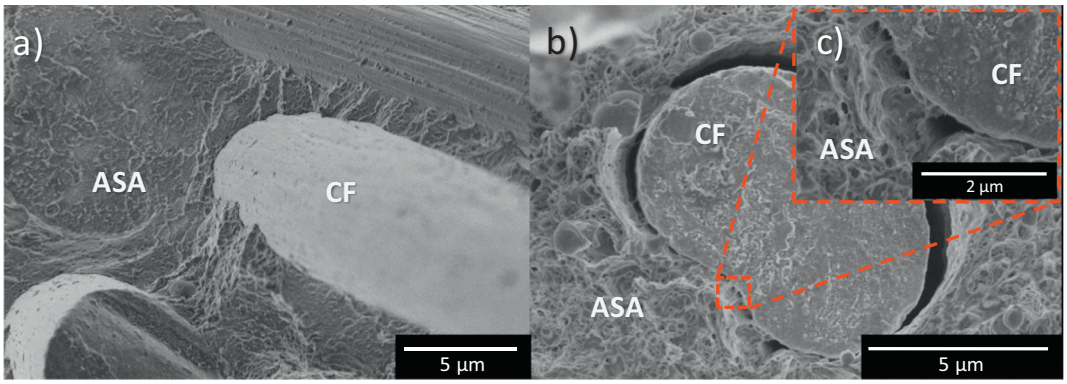

Fig. 6. SEM images of the fracture surface of ASA 20CF after a) flexural fracture at liquid nitrogen temperature (without mechanical test); b) tensile test and c) detail of the bonding interface between ASA and CF.

Table 3
Tensile and flexural results for neat ASA and ASA 20CF along different printing orientations.

Mechanical Properties	Units	Neat ASA		ASA 20CF	
		X	Z	X	Z
Tensile	UTS [MPa]	40.71 ± 1.48	19.1 ± 0.34	60.37 ± 4.22	9.83 ± 0.65
	ε [%]	18.84 ± 0.09	4.31 ± 0.36	1.92 ± 0.08	0.64 ± 0.07
	E [GPa]	1.4 ± 0.1	1.3 ± 0.3	4.5 ± 0.3	1.7 ± 0.1
Flexural	uTSf [MPa]	75.50 ± 0.50	26.6 ± 1	72.0 ± 2.10	15.2 ± 0.9
	εf [%]	4.9 ± 0.1	5.3 ± 0.3	1.4 ± 0.1	1.7 ± 0.1
	Ef [GPa]	2.4 ± 0.1	0.8 ± 0.1	6.2 ± 0.5	0.94 ± 0.04

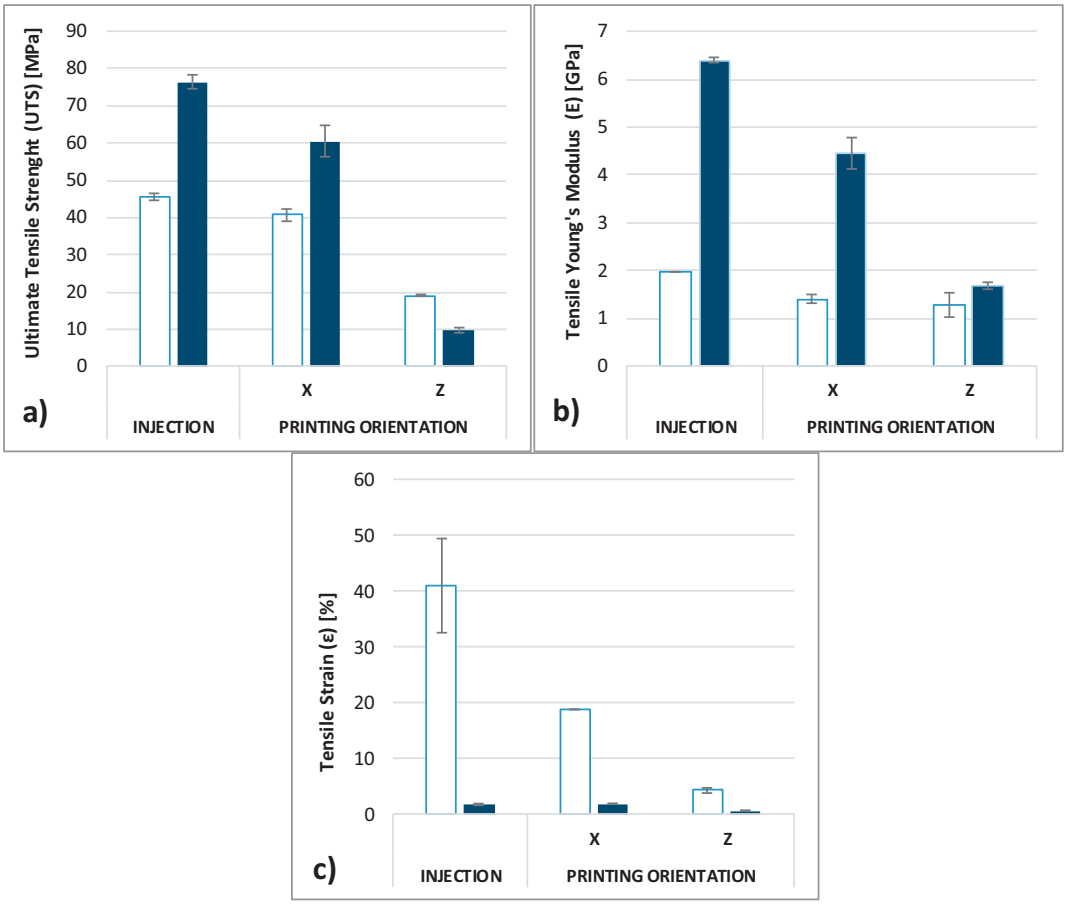

Fig. 7. Comparison (injected vs. printed materials) of the tensile results, a) Strength (UTS); b) Young's modulus (E) and c) Strain (ε). The two different printing directions (X and Z) are indicated. Neat ASA (unfilled bars) and ASA 20CF (filled bars).

Modulus for tension and flexion tests, respectively. The ultimate strength also increases up to 48% and 44% for tension and flexion tests, respectively, while the strain before breaking is reduced (90% for tensile test and 71% for flexural test).

On the contrary, for the Z orientation, the reinforcing character of the filler vanishes and the measured values drop even below the unfilled ASA (ultimate strength and strain in both, tensile and flexural tests). The close results obtained in stiffness compared with unfilled ASA (Young's Modulus for tensile and flexural tests) suggest that the thermoplastic matrix drives the behaviour of the composite under this configuration. Such statement relies on the assumption that the thermoplastic base is the only phase able to bond itself. The physical barrier imposed by the fibers hinders the bonding of the polymer when a new layer is deposited, explaining in part the low tensile strain before breaking for this kind of specimens. The role played by other factors (out of the scope of this work), such as the cooling rate or the presence of voids and porosity on the observed reduction of the mechanical properties should be carefully evaluated.

Chad E. Duty et al. obtained similar anisotropy in tensile results for X and Z orientation using ABS reinforced with CF and GF [27,53]. They also obtained an increment of 13% in Young's modulus over injected ABS 13 wt% CF pieces printed along X orientation, due to the fibers alignment during the extrusion process along this direction. The discrepancies when comparing our results to those reported elsewhere [27,53], for X orientation in reinforced materials, are more likely induced by the dissimilar materials studied and the configuration in test parts. Note that their X tensile specimens were machined from a vertical hexagon part, while in our research, tensile test specimens have been machined from horizontal sheets.

Regarding fracture mechanism, the propagation of crazes occurs through an interlayer in the Z orientation but across the beads for X orientation. These results could be considered as an indication of the effectiveness of the layer-layer bonding and the maximum load that can be reached for each building direction. Fig. 9a) shows the trajectory of the crazes during the fracture in neat ASA in X orientation promoted by a ductile fracture, while for ASA 20CF is not possible to identify that trajectory for the same printing orientation (Fig. 10a) in a fragile fracture.

Figs. 9 and 10 show the presence of different kind of pores for both materials, labelled as Type 1–4. Type 1 pores (see Fig. 9a) and b)), also called inter-bead pores, exhibit a triangular or rhomboidal shape, being the characteristic voids created at the union of adjacent beads during the printing process. These Type 1 pores are directly dependent on the infill pattern, the printing material and the bead thickness employed. With the addition of carbon fibers, the size of these voids is reduced (Fig. 10a) and b)). Halil L. Tekinalp et al. have correlated the addition of carbon fibers with the elimination of die-swell effect during the extrusion process and the increase in thermal conductivity that promotes an accurate bead and a compact structure [51]. Additionally, the effect of the shrinkage reduction with carbon fibers addition must be considered, which avoids significant macroscopic distortions and allows filling the gaps with the outline overlap. The type 2 pores, also called inner-bead pores and pointed in blue in Figs. 9 and 10, are almost spherical, partly induced by the polymer contraction. The porosity observed in ASA 20CF at the interlayers and within the bulk material resemble porosity type 2, but the rougher surface beads at the interlayer creates irregular contact areas resulting in pores classified as type 3, hampering the evaluation of type 2 pores. The addition of CF not only increases

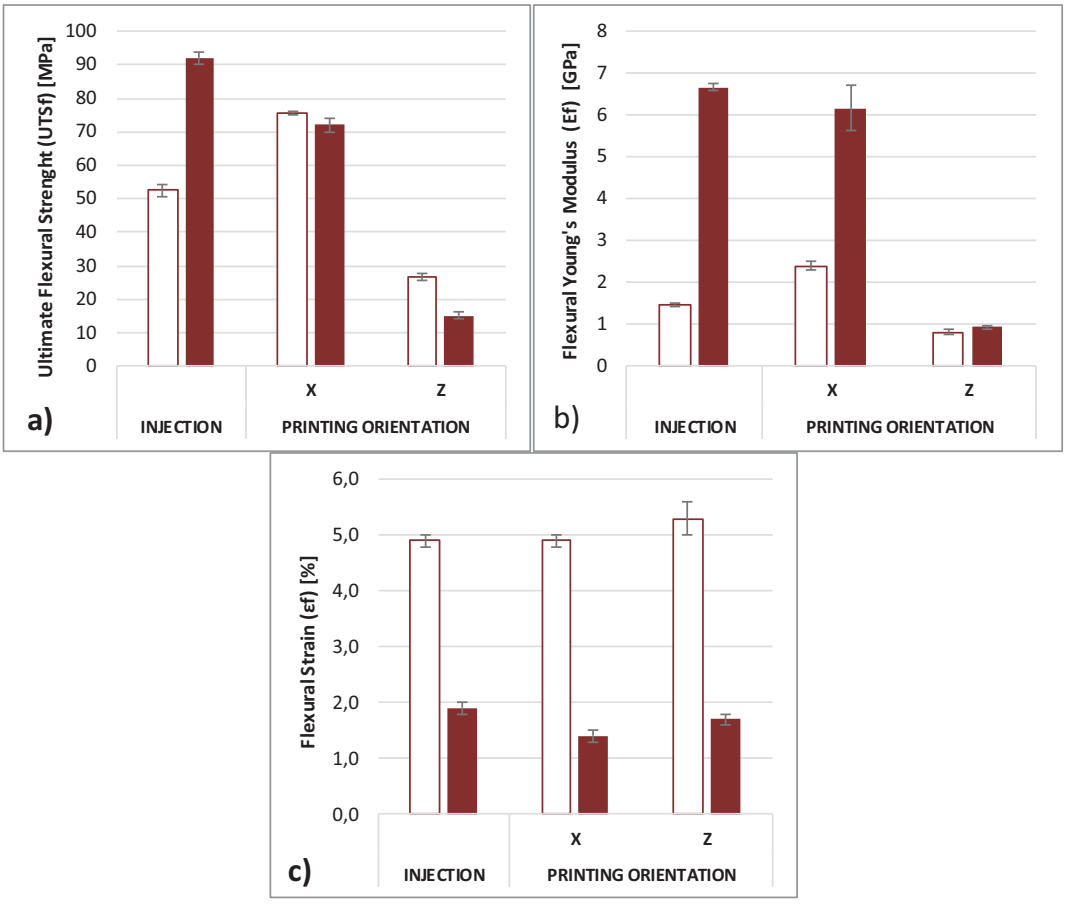

Fig. 8. Comparison of the flexural results, a) Strength (UTSf); b) Young's modulus (Ef) and c) Strain (εf) of injected and printing parts along X and Z orientations, in neat ASA (unfilled bars) and ASA 20CF (filled bars).

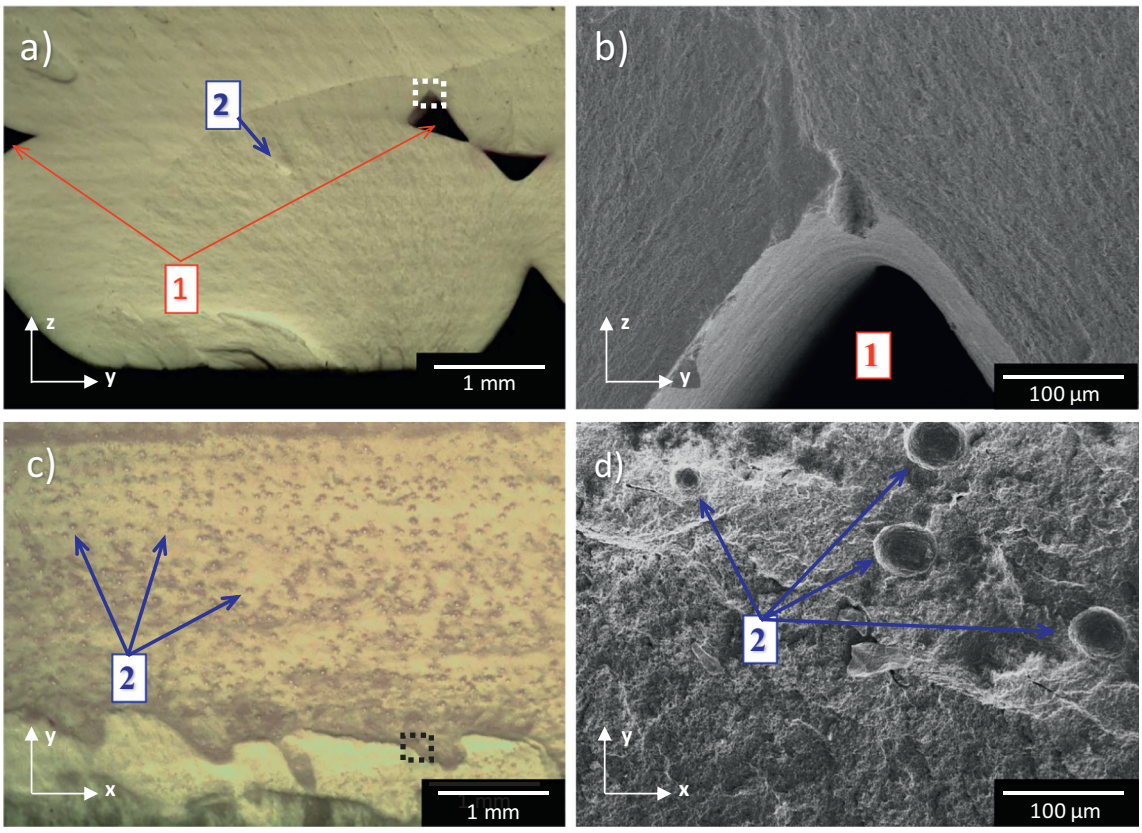

Fig. 9. Optical (a, c) and SEM (b, d) images of fracture surfaces in tensile specimens of neat ASA: a) in X orientation; b) detail of inter-bead porosity in X orientation; c) in Z orientation; d) detail of inner-bead porosity in Z orientation. Black/white arrows represent Cartesian axes; other arrows indicate different kind of porosity (pores of type 1. Inter-bead and type 2. Inner-bead porosity) and red square areas mark on optical micrographs the zones observed by SEM. White lines represent the scale bars.

the roughness of the bead surface, but sometimes produces sharkskin effect, impeding the adhesion between consecutive layers [38,54]. Fig. 10d) displays a SEM image at the transition region between the contact area and the interlayer side of the beads, showing these two kind of porosities, 2 and 3. The type 2 porosity has been previously discussed in bulk reinforced materials, not only for LFAM pieces [27,35,51,] but also for FFF parts [55–58]. Vaxman A. et al. also identified this porosity for extruded materials containing fibers by a double effect of air entrapping

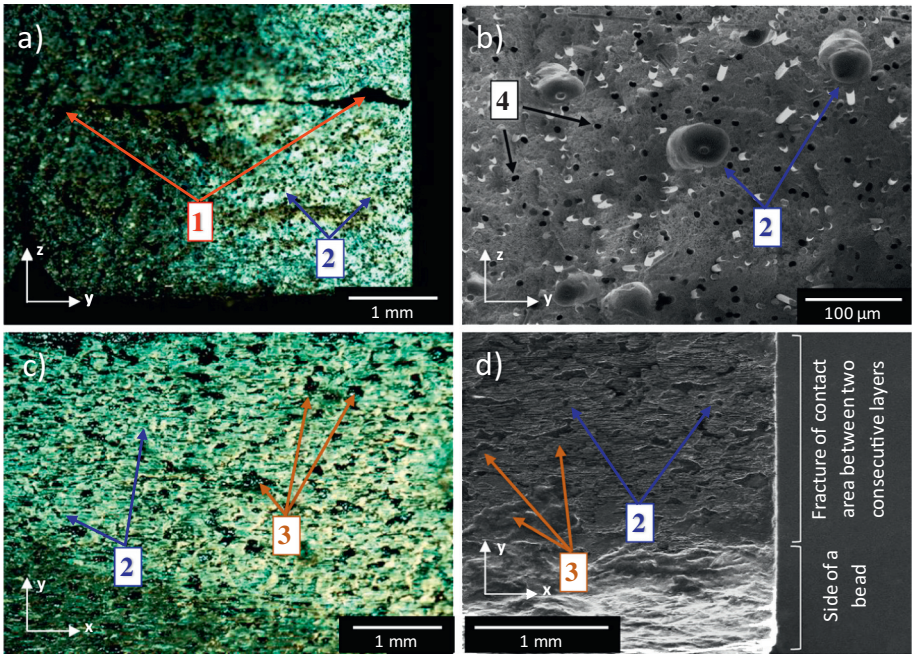

Fig. 10. Optical (a, c) and SEM (b, d) images of the fracture surfaces in ASA 20CF tensile specimens: a) in X orientation; b) detail of the inter-bead and inner-bead porosity in X orientation; c) in Z orientation; d) detail of the fibers in Z orientation. Black/white arrows represent Cartesian axes and other arrows indicate different kind of porosity (pores of type 1. Inter-bead, type 2. Inner-bead, type 3. Roughness porosity and type 4. Pull-out porosity). White lines represent the scale bars.

during mixing and extrusion processes, and by shrink-voids created by an uneven contraction during the melt solidification of the polymer. In addition, they correlate the fiber load, length and cooling rate with the amount and size of pores created. Moreover, the voids appear preferably at the end of the fibers due to different thermal expansion of the phases involved [59]. The type 2 porosity is also observed in neat ASA at the interlayer region, (blue arrows in Fig. 9c) and d)), with only one pore identified within the bulk (Fig. 9a)), while type 3 pores were not detected. Overall, the presence of the type 2 pores might be explained as a consequence of the material contraction in this area, which is the last region that cooled up [60]. Thus, these defects might be considered inherent to the manufacturing process. Finally, type 4 pores (see Fig. 10) are created by the pull-out of fibers during tensile test as reported by Fuda Ning et al. among others [57]. These pores are hardly likely to be created during the printing process, and they must be understood as a result of the tensile stress. The homogeneous CF distribution inside the polymer matrix before the mechanical test, might be responsible for the observed type 4 pores (Fig. 10b).

4. Conclusion

The influence of CF incorporation in ASA has been studied for both, injected and LFAM 3D printed samples. For injected samples, the addition of 20 wt% CF results in an increase of the thermal conductivity (up to 500%) and T_g, while MFR decreases compared with neat ASA. Concerning the mechanical behaviour, the materials have been evaluated by means of tension, flexural and impact tests, pointing to the brittle-like performance of the composites induced by the carbon fibers. A maximum UTS value of 76.3 $\pm$ 1.9 MPa is achieved with the incorporation of the fibers.

Additionally, neat ASA and ASA with 20 wt% CF were successfully printed and their mechanical behaviour was studied along the strongest and weakest orientations (X and Z orientation respectively). A pronounce anisotropy, negligible in injected pieces, is observed in the mechanical properties. A maximum UTS of 60 $\pm$ 4 MPa is achieved for X orientation in ASA CF composite, while the flexural tests results are similar, even higher, than for injected parts. This increase might be attributed to the laminar character of the pieces and the preferential alignment of polymer chains.

Neat ASA specimens show higher strain values than the reinforced composites. The reinforcement effect of CF remains for X orientation but disappear for Z orientation. A prealignment of the fibers along the printing deposition direction was observed; likely imposing a physical barrier in Z direction avoiding polymer diffusion and explaining this behaviour. The addition of CF results in higher roughness porosity and inner-bead porosity, while reducing the inter-bead porosity. The inner-bead is usually considered as an intrinsic defect of extrusion processes, whereas the observed roughness and inter-bead porosity are characteristic of printing procedures.

CRediT authorship contribution statement

Daniel Moreno Sanchez: Conceptualization, Data curation, Formal analysis, Investigation, Writing - original draft. **María de la Mata:** Formal analysis, Writing - original draft, Writing - review & editing. **Francisco Javier Delgado:** Formal analysis. **Víctor Casal:** Funding acquisition, Supervision, Writing - review & editing. **Sergio Ignacio Molina:** Conceptualization, Formal analysis, Funding acquisition, Supervision, Writing - original draft.

Declaration of competing interest

The authors declare that they have no known competing financial interests or personal relationships that could have appeared to influence the work reported in this paper.

Acknowledgements

This work was supported by NAVANTIA company through ADIBUQUE project ('Material-extrusion additive manufacturing technologies applied in building phase of vessels, using compounds thermoplastic materials'), which was co-funded by CTA (Corporación Tecnológica de Andalucía). DMS acknowledges to NAVANTIA and UCA (INNANOMAT research group TEP-946) for supporting his work through the Industrial Doctorate Programme. We would like to thank to A. Flor (NAVANTIA) and F. J. Romalde (CNC Bárcenas) that gave technical support. MdlM acknowledges Ministry of Education for Juan de la Cierva postdoctoral contract.

References

[1] C. W. Hull and C. Arcadia, "United States Patent: Apparatus for production of three-dimensional objects by stereolithography," no. 19, 1984.
[2] R. D'Aveni, The Pan-Industrial Revolution: How New Manufacturing Titans Will Transform the World, 2018th ed., 2018.
[3] J. Smit, S. Kreutzer, C. Moeller, M. Carlberg, Industry 4.0 - study for the ITRE Committee, Eur. Parliam. (2016) 1–94.
[4] F. Calignano, et al., Overview on additive manufacturing technologies, Proc. IEEE 105 (4) (2017) 593–612.
[5] K.V. Wong, A. Hernandez, A review of additive manufacturing, ISRN Mech. Eng 2012 (2012) 1–10.
[6] J. Gardan, Additive manufacturing technologies: state of the art and trends, Addit. Manuf. Handb. Prod. Dev. Def. Ind. 7543 (November) (2017) 149–168.
[7] ASTM-F42.91 Subcommittee, Standard terminology for additive manufacturing technologies, ASTM Des. F2792-12a10.04, 2015.
[8] S.I.S. Scott Crump, United States Patent: US5121329A - Apparatus and method for creating three-dimensional objects, 1989.
[9] M. Fernandez-Vicente, M. Canyada, A. Conejero, Identifying limitations for design for manufacturing with desktop FFF 3D printers, Int. J. Rapid Manuf. 5 (1) (2015) 116–128Dec.
[10] C. Ajinjeru, et al., Determination of melt processing conditions for high performance amorphous thermoplastics for large format additive manufacturing, Addit. Manuf., vol. 21, no. December 2017 (2018) 30222-1.
[11] R. Americas, T.P. Values, LNP ™ THERMOCOMP ™ Am Compound AF004XXAR1, 2017.
[12] D. Moreno Nieto, V. Casal López, S.I. Molina, Large-format polymeric pellet-based additive manufacturing for the naval industry, Addit. Manuf., Vol. 23, No. March (2018) 79–85.
[13] Lonnie J. Love, Cincinnati Big Area Additive Manufacturing (BAAM), 2015.
[14] S. Curran, P. Chambon, R. Lind, L. Love, et al., Big Area Additive Manufacturing and Hardware-in-the-Loop for Rapid Vehicle Powertrain Prototyping: A Case Study on the Development of a 3-D-Printed Shelby Cobra, SAE Technical Paper 2016-01-0328 (2016) https://doi.org/10.4271/2016-01-0328.
[15] C. Hill, et al., Big Area Additive Manufacturing (BAAM) Materials Development and Reinforcement with Advanced Composites, 2018.
[16] P. Chambon, et al., Development of a range-extended electric vehicle powertrain for an integrated energy systems research printed utility vehicle, Appl. Energy 191 (2017) 99–110.
[17] F. Javier, A. Fraga, V. Casal, D.M. Nieto, S.I. Molina, Fabricación Aditiva en la Construcción Naval en el, 2015, 2017 1–6.
[18] A. Ell, D. Nuttall, B. Post, L. Love, A. M. Office, and E. and T. S. Division, Advanced Infusion Techniques With 3-D Printed Tooling, 2016 16.
[19] B. Post, P. Chesser, R. Lind, M. Sallas, L.J. Love, Feasibility of Using Big Area Additive Manufacturing to Directly Manufacture Boat Molds, no. January 2018.
[20] K. Biswas, et al., Big area additive manufacturing applied to buildings, Therm. Perform. Exter. Envel. Whole Build. 2016 (2016)Decem.
[21] L. Love, Explore the Techno-Economic Viability of Using Large-Scale Additive Manufacturing for High-Performance Windows, 2018.
[22] A. Roschli, B.K Post, P.C. Chesser, M. Sallas, L.J. Love, K.T Gaul, Precast concrete molds fabricated with big area additive manufacturing, Proceedings of the 29th Int, Solid Free. Fabr. Symp. (2018) 568–579.
[23] K. Biswas, et al., Additive manufacturing integrated energy—enabling innovative solutions for buildings of the future, J. Sol. Energy Eng 139 (1) (2016), 015001.
[24] M. Mann, et al., The Current State of Additive Manufacturing in Wind Energy Systems, no. September 2017.
[25] B. Post, et al., Additive Manufacturing of Wind Turbine Molds, no. June 2017.
[26] B. Richardson, BAAM Additive Manufacturing of a Building Integrated Wind Turbine for Mass Production, 2018.
[27] C.E. Duty, et al., Structure and mechanical behavior of big area additive manufacturing (BAAM) materials, Rapid Prototyp. J. 23 (1) (2017) 181–189.
[28] C. Duty, J. Failla, S. Kim, T. Smith, J. Lindahl, V. Kunc, Z-pinning approach for 3D printing mechanically isotropic materials ☆, Addit. Manuf., Vol. 27, No. March (2019) 175–184.
[29] A. Roschli, Increasing interlaminar strength in large scale additive manufacturing, Proceedings of the 29th Int, Solid Free. Fabr. Symp. (2018) 543–555.
[30] V. Kishore, et al., Infrared preheating to improve interlayer strength of big area additive manufacturing (BAAM) components, Addit. Manuf 14 (2017) 7–12.
[31] H. Narahara, Y. Shirahama, H. Koresawa, Improvement and evaluation of the interlaminar bonding strength of FDM parts by atmospheric-pressure plasma, Procedia CIRP 42 (2016) 754–759Isem Xviii.

[32] J. Du, Z. Wei, X. Wang, J. Wang, Z. Chen, An improved fused deposition modeling process for forming large-size thin-walled parts, J. Mater. Process. Technol. 234 (2016) 332–341.
[33] B.A. Lackey, et al., Welding of 3D-printed carbon nanotube–polymer composites by locally induced microwave heating, Sci. Adv. 3 (6) (2017), e1700262.
[34] C. Duty, et al., A viscoelastic model for extrusion-based 3D printing of polymers what makes a material printable? J. Manuf. Process., Vol. Submitted, No. 2017 (2017) 526–537August.
[35] C.E. Duty, T. Drye, A. Franc, Material development for tooling applications using big area additive manufacturing (BAAM), ORNL Tech. Rep. (2015) 1–8ORNL/TM-2015/78.
[36] L.J. Love, et al., The importance of carbon fiber to polymer additive manufacturing, J. Mater. Res. 29 (17) (2014) 1893–1898.
[37] E. Yasa, K. Ersoy, in: Eskişehir (Ed.), Additive Manufacturing of Polymer Matrix Composites, Aircraft Technology, Melih Cemal Kuşhan 2018, pp. 147–169.
[38] A.A. Hassen, J. Lindahl, X. Chen, B. Post, L. Love, V. Kunc, Additive manufacturing of composite tooling using high temperature thermoplastic materials, Int. SAMPE Tech. Conf. (2016) 1–11Sku/Code: LB15–0335.
[39] V. Kishore, et al., Additive manufacturing of high performance semicrystalline thermoplastics and their composites, Solid Free. Fabr. Symp. Proc. (2016) 906–915no. November.
[40] B. Xiang, J. Zhang, Effects of content and surface hydrophobic modification of BaTiO3 on the cooling properties of ASA (acrylonitrile-styrene-acrylate copolymer), Appl. Surf. Sci. 427 (2018) 654–661.
[41] J. Scheirs, D. Priddy, D.P. John Scheirs, Modern Styrenic Polymers: Polystyrenes and Styrenic Copolymers, Wiley, 2003.
[42] J. Song, X. Liu, Y. Zhang, B. Huang, W. Yang, Carbon-fiber-reinforced acrylonitrile-styrene-acrylate composites: mechanical and rheological properties and electrical resistivity, J. Appl. Polym. Sci. 133 (13) (2016) 2–7.
[43] Footage of world's largest plastic 3D printer printing pedestrian bridge, [Online]. Available: https://www.3ders.org/articles/20181116-footage-of-worlds-largest-plastic-printer-printing-pedestrian-bridge.html 2019.
[44] M. Längauer, K. Liu, C. Kneidinger, G. Schaffler, B. Purgleitner, G. Zitzenbacher, Experimental analysis of the influence of pellet shape on single screw extrusion, J. Appl. Polym. Sci. 132 (13) (2015) 1–9.
[45] R.C. Bansal, Carbon Fibers Carbon Fibers, 2008.
[46] S.Y. Fu, B. Lauke, E. Mäder, C.Y. Yue, X. Hu, Tensile properties of short-glass-fiber- and short-carbon-fiber-reinforced polypropylene composites, Compos. Part A Appl. Sci. Manuf 31 (10) (2000) 1117–1125.
[47] P. Parandoush, D. Lin, "A review on additive manufacturing of polymer-fiber composites," Composite Structures, vol, 182. Elsevier Ltd (2017) 36–53.
[48] S.I.M.D. Moreno-Sanchez, V. Casal, Desarrollo de materiales compuestos de base ASA para Fabricación Aditiva de Gran Formato, Mater. Compuestos 3 (3) (2019) 91–94.
[49] B.G. Compton, B.K. Post, C.E. Duty, L. Love, V. Kunc, Thermal analysis of additive manufacturing of large-scale thermoplastic polymer composites, Addit. Manuf 17 (2017) 77–86.
[50] Q. Sun, G.M. Rizvi, C.T. Bellehumeur, P. Gu, Effect of processing conditions on the bonding quality of FDM polymer filaments, Rapid Prototyp. J. 14 (2) (2008) 72–80.
[51] H.L. Tekinalp, et al., Highly oriented carbon fiber-polymer composites via additive manufacturing, Compos. Sci. Technol. 105 (2014) 144–150.
[52] A. Roschli, et al., Designing for big area additive manufacturing, Addit. Manuf. 25 (2018) (2019) 275–285no. September.
[53] L.J. Love, et al., Breaking barriers inpolymer additive manufacturing, International SAMPE Technical Conference, 2015.
[54] V. Kishore, et al., "Predicting sharkskin instability in extrusion additive manufacturing of reinforced thermoplastics," Solid Free, Fabr. Symp. (2017) 1696–1704.
[55] Z. Quan, et al., Microstructural design and additive manufacturing and characterization of 3D orthogonal short carbon fiber/acrylonitrile-butadiene-styrene preform and composite, Compos. Sci. Technol. 126 (2016) 139–148.
[56] J. Gelb, A. Karakoç, Ö. Keleş, J. Freund, J. Huynh, E.H. Anderson, Stochastic fracture of additively manufactured porous composites, Sci. Rep. 8 (1) (2018).
[57] F. Ning, W. Cong, J. Qiu, J. Wei, S. Wang, Additive manufacturing of carbon fiber reinforced thermoplastic composites using fused deposition modeling, Compos. Part B Eng 80 (2015) 369–378.
[58] Z. Li, Y. Li, Wang, Flexural properties and fracture behavior of CF/PEEK in orthogonal building orientation by FDM: microstructure and mechanism, Polymers (Basel). 11 (4) (2019) 656.
[59] A. Vaxman, M. Narkis, A. Siegmann, S. Kenig, Void formation in short-fiber thermoplastic composites, Polym. Compos. 10 (6) (1989) 449–453.
[60] C. Rauwendaal, Understanding Extrusion, 2nd Revise, Hanser Publications, Cincinnati, 2010.